

Tunable coherent microwave beam splitter and combiner at the single-photon level

Y.-H. Huang,¹ K.-M. Hsieh,² F. Aziz,¹ Z. Q. Niu,^{3,4} P. Y. Wen,⁵ Y.-T. Cheng,² Y.-S. Tsai,¹ J. C. Chen,^{1,6} Xin Wang,² A. F. Kockum,⁷ Z.-R. Lin,^{3, a)} Y.-H. Lin,^{1, 6, a)} and I.-C. Hoi^{1, 2, a)}

¹⁾*Department of Physics, National Tsing Hua University, Hsinchu 30013, Taiwan*

²⁾*Department of Physics, City University of Hong Kong, Kowloon, Hong Kong SAR 999077, China*

³⁾*State Key Laboratory of Materials for Integrated Circuits, Shanghai Institute of Microsystem and Information Technology, Chinese Academy of Sciences, Shanghai 200050, China*

⁴⁾*ShanghaiTech University, Shanghai 201210, China*

⁵⁾*Department of Physics, National Chung Cheng University, Chiayi 621301, Taiwan*

⁶⁾*Center for Quantum Technology, National Tsing Hua University, Hsinchu 30013, Taiwan*

⁷⁾*Department of Microtechnology and Nanoscience, Chalmers University of Technology, 412 96 Gothenburg, Sweden*

(Dated: 27 March 2025)

A beam splitter is a key component used to direct and combine light paths in various optical and microwave systems. It plays a crucial role in devices like interferometers, such as the Mach–Zehnder and Hong–Ou–Mandel setups, where it splits light into different paths for interference measurements. These measurements are vital for precise phase and coherence testing in both classical and quantum optical experiments. In this work, we present a nonlinear beam splitter and beam combiner utilizing a frequency-tunable superconducting artificial atom in a one-dimensional open waveguide. This beam splitter is highly versatile, with adjustable transparency ranging from unity to zero for signals at the single-photon level. Additionally, the beam combiner can merge two coherent beams, generating interference fringes as the relative phase between them varies.

Beam splitters and combiners are fundamental optical and microwave components that manipulate light by either splitting an incoming beam into two paths or merging them into a single one. In linear optical quantum computing (LOQC)^{1–7}, beam splitters and combiners are crucial building blocks for implementing quantum logic gates using photons; any unitary $N \times N$ matrix can be implemented with an array of fewer than $N^2/2$ beam-splitters and some phase shifters^{8,9}. Beam combiners are essential for observing the Hong–Ou–Mandel effect¹⁰, which plays a significant role in verifying photon indistinguishability. In interferometry, beam splitters divide light beams into separate paths, allowing them to interfere upon recombination and enabling high-precision measurements of distances^{11,12}, surface profiles¹³, and even gravitational waves^{14,15}. A classic example of their application in precision metrology is the Mach–Zehnder interferometer¹⁶ (MZI), which relies on beam splitters and beam combiners to achieve interference-based measurements.

In the search for significant light-matter interactions that can aid LOQC, superconducting circuits^{17,18}, often referred to as artificial atoms, offer a distinctive and versatile platform for implementing beam splitters and combiners at microwave frequencies. A significant advantage of these circuits, which have been considered for LOQC¹⁹, is the ability to engineer and customize the parameters of artificial atoms and the light-matter interaction. Recent efforts have focused on achieving strong coupling between superconducting artificial atoms

and propagating microwave photons, leading to the emergence of waveguide quantum electrodynamics (wQED)^{20,21} with superconducting qubits. This field has seen remarkable advances, including resonance fluorescence²², photon routing²³, non-classical microwaves²⁴, Landau–Zener–Stückelberg–Majorana interferometry²⁵, cross-Kerr effect between two fields²⁶, lifetime control of artificial atoms²⁷, atom-field interaction control via phase shaping²⁸, amplification without population inversion²⁹, collective Lamb shift between two superconducting qubits³⁰, coherent dynamics of a photon-dressed qubit³¹, giant atoms³², photon-mediated interactions between atoms³³, deterministic photon loading³⁴, etc.

These pioneering experiments have inspired new directions in demonstrating microwave components for interferometers within the framework of wQED using superconducting circuits. In this framework, beam splitting has been achieved¹⁷ with, e.g., two transmission lines close to each other³⁵, a 90- or 180-degree hybrid coupler^{36,37}, a Wilkinson power divider^{37,38}, or a three-wave mixer with Josephson junctions³⁹. However, these approaches tend to suffer from requiring complicated setups or lacking tunability.

In this Letter, we demonstrate a transmon qubit⁴⁰, an artificial atom, functioning as a simple tunable beam splitter and combiner. A few theoretical works have considered using such an artificial atom⁴¹, or an artificial atom coupled to a cavity⁴², as a beam splitter for single microwave photons. In Ref.²³, Hoi *et al.* demonstrated experimentally the transmittance and reflectance of a transmon as a function of control pulse power, accompanied by incoherent loss that led to a very lossy beam splitter. Here, we engineer a transmon qubit to function as a highly efficient, negligible-loss beam splitter with tunable transparency controlled by adjusting an external magnetic flux. Additionally, we engineer the transmon qubit

^{a)} Authors to whom correspondence should be addressed:

zrlin@mail.sim.ac.cn;

yhlin@phys.nthu.edu.tw;

iochoi@cityu.edu.hk

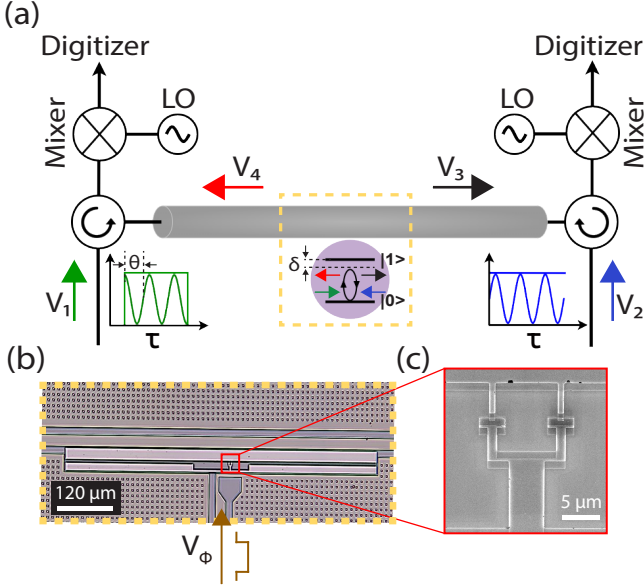


FIG. 1. The experimental scheme and device. (a) A simplified schematic of the experiment (see Fig. S1 in the Supplementary Material for details). An artificial atom (purple disk inside the yellow dashed square) is embedded in a 1D open transmission line. Two input waves, V_1 (green arrow) and V_2 (blue arrow), with a carrier frequency detuned by δ from the resonance frequency of the atom, can be simultaneously applied to the atom. The output signals V_3 (black arrow) and V_4 (red arrow) are down-converted by a local oscillator (LO) and recorded by a digitizer. (b) Optical micrograph of the device. A transmon qubit (light gray) is capacitively coupled to a 1D open transmission line (dark gray). The red square indicates the SQUID. (c) Scanning electron micrograph of the SQUID.

$\omega/2\pi$	$\Gamma/2\pi$	$\Gamma^n/2\pi$	$\gamma/2\pi$	ϕ
[GHz]	[MHz]	[MHz]	[MHz]	[rad]
4.1108	22.15	0.39	11.47	0.0526

TABLE I. Extracted qubit parameters from single-tone spectroscopy. The detailed experimental setup is described in Fig. S1 of the Supplementary Material.

to combine two incoming coherent light beams, producing an interference pattern that varies with the relative phase between the two incoming beams. These findings demonstrate the potential of superconducting circuits for driving the development of microwave-based MZIs and advancing quantum computing with linear optical systems.

Fig. 1(a) illustrates the configuration for our on-chip beam splitter and combiner. The device incorporates a transmon qubit with a superconducting quantum interference device (SQUID) loop, capacitively coupled to the center of a one-dimensional (1D) open transmission line. We first characterize our device using transmission spectroscopy to extract the essential parameters at the qubit's resonance frequency $\omega/2\pi = 4.1108$ GHz (see Table I) for time-domain measurements and simulation. Here, Γ and $\gamma = \Gamma/2 + \Gamma^n$ are the relaxation and decoherence rates, respectively; the non-radiative decoherence rate Γ^n (including pure dephasing and intrinsic

loss) is much smaller than Γ . The detailed characterization method is given in Sec. S2 of the Supplementary Material.

For the beam-splitter operation, a single input field [denoted V_1 , indicated by the green arrow in Fig. 1(a)] is introduced. A cryogenic microwave circulator directs this field and facilitates its interaction with the two-level system (atom), as indicated by the yellow dashed box in Fig. 1(a). We then measure the resulting transmitted (V_3 , black arrow) and reflected (V_4 , red arrow) output fields via heterodyne detection. In the beam combiner operation, two input fields, V_1 and V_2 , are introduced with a phase θ in V_1 that can be varied. The combined fields are again the outgoing fields V_3 and V_4 .

The mathematical representation of the reciprocal beam splitter and beam combiner is a 2×2 matrix⁴⁴ relating the output fields (V_3, V_4) to the input fields (V_1, V_2) as a function of the phase θ and the time τ :

$$\begin{pmatrix} V_3 \\ V_4 \end{pmatrix} = \begin{pmatrix} t_L & r_R \\ r_L & t_R \end{pmatrix} \begin{pmatrix} V_1 \\ V_2 \end{pmatrix}, \quad (1)$$

$$V_1(\theta, \tau) = V_{1,\text{off}} e^{i(\omega_p \tau + \theta + \theta_0)}, \quad (2)$$

$$V_2(\tau) = V_{2,\text{off}} e^{i\omega_p \tau}. \quad (3)$$

Here, $V_{1,\text{off}}$ and $V_{2,\text{off}}$ represent the bare on-chip amplitudes of the incoming waves without any interaction with the qubit and θ_0 is the initial phase difference between V_1 and V_2 . The calibration of these parameters is described in Sec. S3 in the Supplementary Material.

The transmission coefficient t and reflection coefficient r ⁴⁵ are given by

$$t = 1 + r, \quad (4)$$

$$r = -e^{i\phi} \frac{\Gamma}{2\gamma} \frac{1 - i\frac{\delta}{\gamma}}{1 + \left(\frac{\delta}{\gamma}\right)^2 + \frac{\Omega^2}{\gamma^2}}. \quad (5)$$

Here, $\delta = \omega_p - \omega$, is the detuning between the qubit frequency ω and the probe frequency ω_p , Ω is the Rabi frequency, and ϕ is the impedance mismatch angle. The subscripts R and L in Eq. (1) refer to inputs on the right side and the left side of the qubit, respectively. Ideally, when both the transmittance $|t|^2 = T$ and the reflectance $|r|^2 = R$ are 0.5, maximum or minimum visibility will be observed depending on whether the interference is constructive or destructive as the relative phase θ changes.

We now explore the qubit's functionality as a beam splitter using a time-domain setup [see Fig. 1(a)]. A pulse [green in the inset of Fig. 2(a)] with $\omega_p/2\pi = 4.1108$ GHz [orange arrow in Fig. 2(a)] is applied to the qubit. In this experiment, we control the resonance frequency ω of the artificial atom by applying an external flux V_Φ [see Fig. 1(b)]. As seen in Fig. 2(a), the artificial atom exhibits near 100% (0%) reflectance (transmittance) when the input is exactly resonant ($\delta = 0$). Conversely, when the atom is far detuned, it becomes off-resonant ($|\delta| \gg \gamma$) with the incoming wave, resulting in no interaction, where $T \sim 100\%$ and $R \sim 0\%$. Nearly resonant tuning ($|\delta| \sim \gamma$) within the qubit's linewidth results in partial transmittance and partial reflectance.

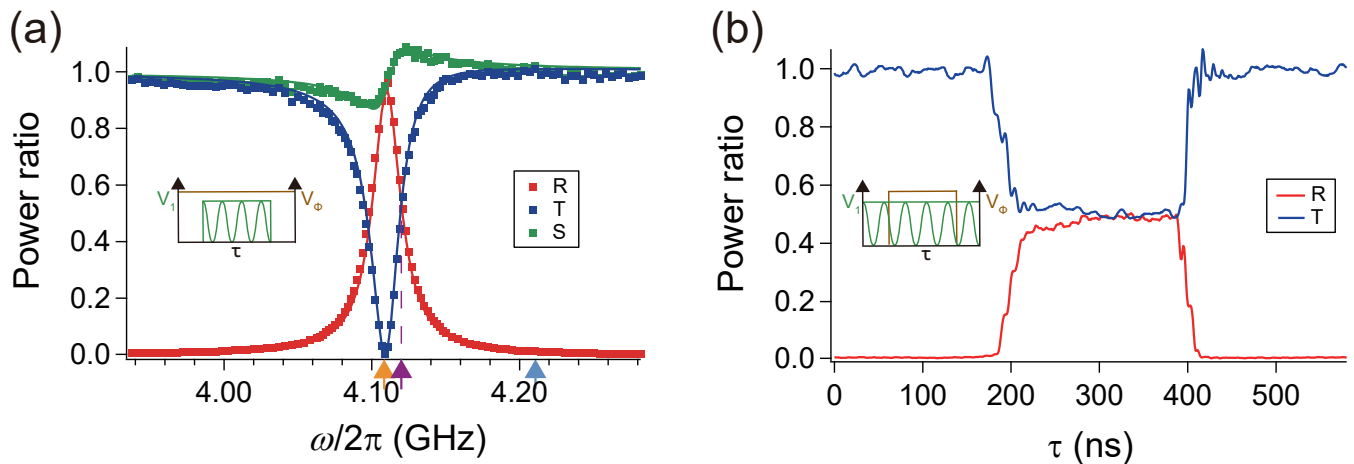


FIG. 2. A tunable beam splitter. (a) We apply a weak pulse as input (green wave in the inset) and record the transmittance T and reflectance R . We set $\omega_p/2\pi = 4.1108$ GHz (orange arrow) and vary $\omega/2\pi$ by applying a global flux V_ϕ (brown wave in the inset) to manipulate the transparency of the qubit. The red (blue) dots are the reflectance (transmittance) data, which are the averages of the steady-state region across the pulse at different $\omega/2\pi$. The green dots S are the sum of the reflectance and the transmittance. The solid curves represent the theoretical predictions, according to Eqs. (4) and (5), with each curve matching a corresponding color. (b) Transmittance and reflectance using a continuous-wave input (green wave in the inset) with $\omega_p/2\pi = 4.1108$ GHz [orange arrow in Fig. 2(a)]. A Gaussian square pulse (brown wave in the inset) serves as a flux pulse to rapidly tune the qubit from $\omega/2\pi = 4.2108$ GHz [cyan arrow in Fig. 2(a)] to $\omega/2\pi = 4.12$ GHz [purple arrow in Fig. 2(a)]. With these settings, we observe a ratio of reflectance and transmittance around 50:50 during the square pulse.

In Fig. 2(a), the blue and red dots are experimental data averaged over the steady-state region in the output pulses, while the solid curves are theoretical fits using Eqs. (4) and (5), showing good agreement. The green dots and curve depict the experimental data and theoretical fit of the sum of transmittance and reflectance ($S = T + R$), respectively. In the vicinity of the resonance frequency, we see $S \neq 1$, which we attribute to impedance mismatch ($\phi \neq 0$) from the transmission line.

The data in Fig. 2(a) show that the qubit functions as a tunable beam splitter, with transparency that can be adjusted from unity to zero by tuning the external flux. Furthermore, applying a flux pulse [brown in the inset of Fig. 2(b)] to rapidly tune the qubit from $\omega/2\pi = 4.2108$ GHz [cyan arrow in Fig. 2(a)] to $\omega/2\pi = 4.12$ GHz [purple arrow in Fig. 2(a)] achieves a 50 : 50 ratio of transmittance and reflectance, demonstrating the transparency tunability within a few nanoseconds. The flux-pulse amplitude can be adjusted to modify T and R (see Fig. S4 in the Supplementary Material for details).

Next, we investigate the qubit's functionality as a beam combiner. We set the qubit's resonance frequency to $\omega/2\pi = 4.12$ GHz [purple arrow in Fig. 2(a)], achieving a transmittance to reflectance ratio of approximately 50 : 50. Two weak probes V_1 and V_2 at $\omega_p/2\pi = 4.1108$ GHz are simultaneously applied to the atom. The output signals oscillate as a function of the phase θ of V_1 , as shown in Fig. 3(a). In Fig. 3(a), the blue and red dots represent the experimental data V_3 and V_4 , while the solid curves of corresponding colors are the theoretical predictions based on Eqs. (1)–(5) (see Sec. S4 in the Supplementary Material for details; the scattering-matrix elements are summarized in Table II).

When the qubit is far detuned, as shown by the purple (gray) dots for V_3 (V_4), the input fields no longer interact with the

qubit, resulting in no interference between the two input fields. This is evident as the pink and cyan dots in Fig. 3(a), where these single-tone data remain constant irrespective of changes in θ . Imperfect isolation of the cryogenic microwave circulator causes leakage signals, mitigated using a phase shifter, tunable attenuator, and directional coupler (see Sec. S1 in the Supplementary Material), with results shown by the wheat and green dots at negligible constant levels in Fig. 3(a).

Above, we examined the beam combiner with $T \sim 0.5$, where the qubit was subjected to low probe power. Now, we increase the input pulse power by 45 dB, from low to high such that $\Omega \gg \gamma$, while keeping all other parameters unchanged. In this configuration, the field is primarily transmitted, since the artificial atom is almost saturated, and only a weak interference pattern is observed, as shown in Fig. 3(b), with reduced visibility compared to the results in Fig. 3(a). However, the remaining oscillations in the blue (V_3) and red (V_4) data points indicate that the high probe power does not completely saturate the qubit. To confirm this observation, we conducted an experiment with a far-detuned qubit (i.e., without qubit interaction), which revealed identical power levels in the output signals V_3 and V_4 , with no interference effects present [see purple and gray data in Fig. 3(b)].

In conclusion, we have demonstrated that a transmon qubit in a 1D open transmission line can function as a nonlinear beam splitter and combiner at the single-photon level in the microwave regime. By adjusting an external magnetic field, we can tune the qubit's resonance frequency and modify the ratio of transmittance and reflectance of the interacting light. In this way, we can also widely adjust the working frequency range. Additionally, we showed that we can combine two incoming coherent lights, with interference fringes appearing as

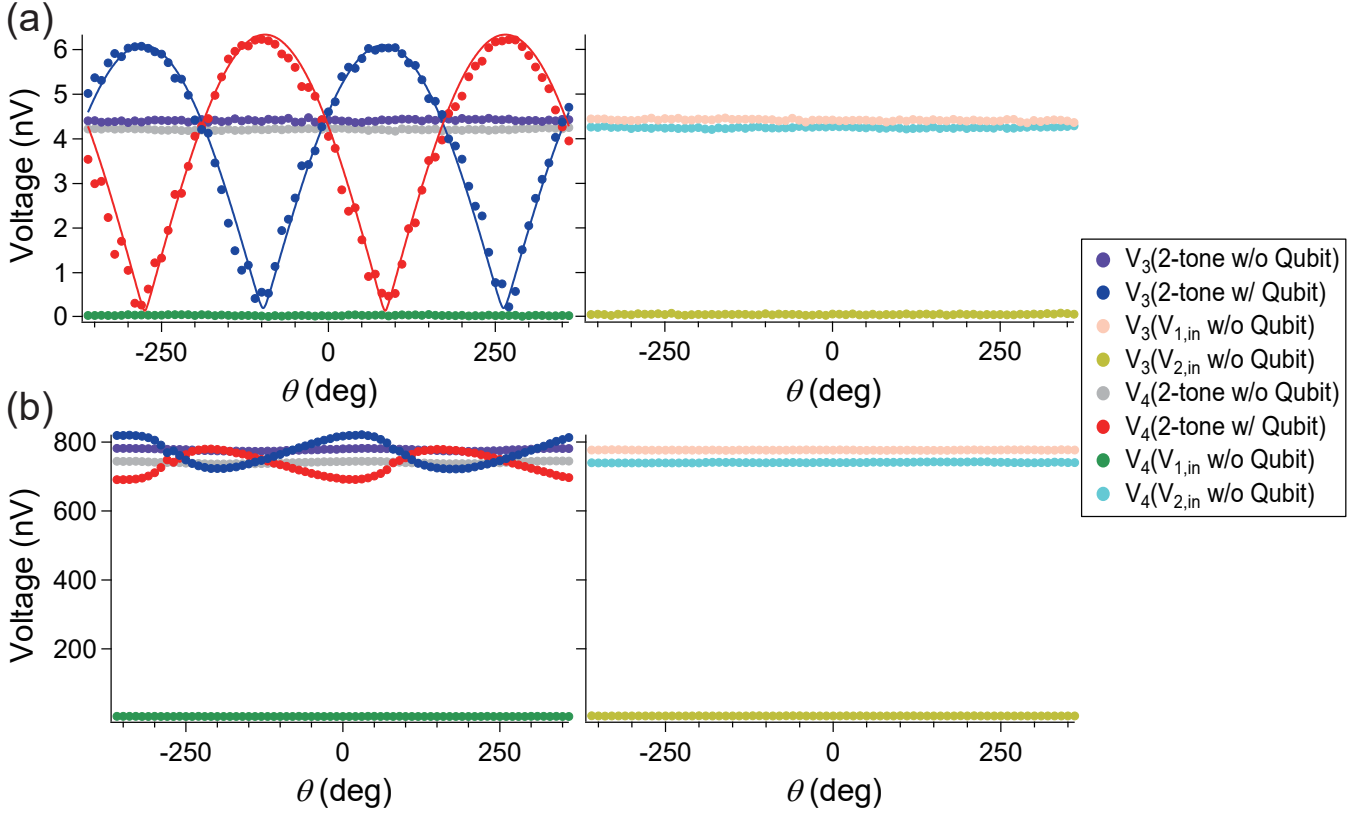


FIG. 3. A nonlinear tunable beam combiner. (a) When the qubit is tuned to $\omega/2\pi = 4.12$ GHz [purple arrow in Fig. 2(a)], the ratio of reflectance and transmittance is around 50:50. Two weak input waves, V_1 [green arrow in Fig. 1(a)] and V_2 [blue arrow in Fig. 1(a)] with $\omega_p/2\pi = 4.1108$ GHz, are simultaneously sent to the qubit. The output signals oscillate as a function of the phase θ of V_1 [as defined in Fig. 1(a)]. The blue \bullet and red \bullet data are the experimental data when the qubit is tuned to $\omega/2\pi = 4.12$ GHz; the solid curves with the corresponding colors are the theory predictions from Eqs. (1)–(5) using the parameters in Table II. The purple \bullet (gray \bullet) data are the V_3 (V_4) signals when the qubit is far detuned. The pink \bullet (green \bullet) data are the V_3 (V_4) signals when the qubit is far detuned and there only V_1 is applied to the qubit. The wheat \bullet (cyan \bullet) data are the V_3 (V_4) signals when the qubit is far detuned and only V_2 is applied to the qubit. (b) In the same setup as shown in Fig. 3(a), but with increased probe power ($\Omega \gg \gamma$), the interference visibility decreases dramatically. The remaining oscillations indicate that the high probe power does not completely saturate the qubit.

$V_{1,off}$ [nV]	$V_{2,off}$ [nV]	t_L	r_R	r_L	t_R	θ_0 [rad]
$4.261 + 1.129i$	$2.182 + 3.634i$	-	$-0.387 + 0.577i$	$-0.707 + 0.203i$	$-0.010 + 0.730i$	1.152

TABLE II. Scattering-matrix elements at $\omega_p/2\pi = 4.1108$ GHz and $\omega/2\pi = 4.12$ GHz for Fig. 3(a). See Sec. S4 in the Supplementary Material for details.

a function of the relative phase between them. These results highlight the robustness, simplicity, and versatility of a superconducting artificial atom as both a beam splitter and combiner, which are critical components of quantum-technology applications such as MZIs or LOQC.

See the Supplementary Material for details on the schematic of the experimental setup, qubit characterization via the single-tone spectroscopy, calibration measurement of the required parameters, scattering matrix elements calculation, and the detailed data for Fig. 2(b) and Fig. 3(a).

ACKNOWLEDGMENTS

I.-C.H. acknowledges financial support from City University of Hong Kong project 9610617, from the Research Grants Council of Hong Kong (Grant No. 11307324) and from Guangdong Provincial Quantum Science Strategic Initiative (Grant No. GDZX2203001, GDZX2303005, GDZX2403001). AFK acknowledges support from the Swedish Foundation for Strategic Research (grant numbers FFL21-0279 and FUS21-0063), the Horizon Europe programme HORIZON-CL4-2022-QUANTUM-01-SGA via the project 101113946 OpenSuperQPlus100, and from the Knut and Alice Wallenberg Foundation through the Wallenberg

Centre for Quantum Technology (WACQT).

AUTHOR DECLARATIONS

Conflict of Interest

The authors have no conflicts to disclose.

Author Contributions

Y.-H. Huang, K.-M. Hsieh, F. Aziz and Z. Q. Niu contributed equally to this work.

Y.-H. Huang: Conceptualization (equal); Data curation (lead); Writing - original draft (equal); Writing - review & editing (equal); Methodology (equal); Formal analysis (equal). **K.-M. Hsieh:** Conceptualization (equal); Data curation (lead); Writing - original draft (equal); Writing - review & editing (equal); Methodology (equal); Formal analysis (equal). **F. Aziz:** Conceptualization (equal); Data curation (equal); Writing - original draft (equal); Writing - review & editing (equal). **Z. Q. Niu:** Conceptualization (equal); Resources (equal); Writing - review & editing (equal). **P. Y. Wen:** Conceptualization (equal). **Y.-T. Cheng:** Conceptualization (equal); Software (lead). **Y.-S. Tsai:** Conceptualization (equal). **J. C. Chen:** Conceptualization (equal). **Xin Wang:** Writing - review & editing (equal); Funding acquisition (equal). **A. F. Kockum:** Conceptualization (equal); Writing - review & editing (equal); Funding acquisition (equal). **Z.-R. Lin:** Conceptualization (equal); Resources (equal); Supervision (equal). **Y.-H. Lin:** Conceptualization (equal); Supervision (equal). **I.-C. Hoi:** Conceptualization (equal); Supervision (lead); Writing - review & editing (equal); Project administration (lead); Funding acquisition (equal).

DATA AVAILABILITY

The data that support the findings of this study are available from the corresponding author upon reasonable request.

REFERENCES

- ¹E. Knill, R. Laflamme, and G. J. Milburn. A scheme for efficient quantum computation with linear optics. *Nature*, 409:46–52, 2001.
- ²S. L. Braunstein and P. van Loock. Quantum information with continuous variables. *Reviews of Modern Physics*, 77:513, 2005.
- ³P. Kok, W. J. Munro, K. Nemoto, T. C. Ralph, J. P. Dowling, and G. J. Milburn. Linear optical quantum computing with photonic qubits. *Reviews of Modern Physics*, 79:135, 2007.
- ⁴Peter P Rohde. Optical quantum computing with photons of arbitrarily low fidelity and purity. *Physical Review A*, 86:052321, 2012.
- ⁵Stefano Paesani, Jacob FF Bulmer, Alex E Jones, Raffaele Santagati, and Anthony Laing. Scheme for universal high-dimensional quantum computation with linear optics. *Physical Review Letters*, 126:230504, 2021.
- ⁶Lars S Madsen, Fabian Laudenbach, Mohsen Falamarzi Askarani, Fabien Rortais, Trevor Vincent, Jacob FF Bulmer, Filippo M Miatto, Leonhard Neuhaus, Lukas G Helt, Matthew J Collins, et al. Quantum computational advantage with a programmable photonic processor. *Nature*, 606:75–81, 2022.
- ⁷TM Graham, Y Song, J Scott, C Poole, L Phuttitarn, K Jooya, P Eichler, X Jiang, A Marra, B Grinkemeyer, et al. Multi-qubit entanglement and algorithms on a neutral-atom quantum computer. *Nature*, 604:457–462, 2022.
- ⁸M. Reck, A. Zeilinger, H. J. Bernstein, and P. Bertani. Experimental realization of any discrete unitary operator. *Physical Review Letters*, 73:58, 1994.
- ⁹A. Bouland and S. Aaronson. Generation of universal linear optics by any beam splitter. *Physical Review A*, 89:062316, 2014.
- ¹⁰Chong-Ki Hong, Zhe-Yu Ou, and Leonard Mandel. Measurement of sub-picosecond time intervals between two photons by interference. *Physical Review Letters*, 59:2044, 1987.
- ¹¹Joohyung Lee, Seongheum Han, Keunwoo Lee, Eundeok Bae, Seungman Kim, Sanghyun Lee, Seung-Woo Kim, and Young-Jin Kim. Absolute distance measurement by dual-comb interferometry with adjustable synthetic wavelength. *Measurement Science and Technology*, 24:045201, 2013.
- ¹²Ruitao Yang, Florian Pollinger, Karl Meiners-Hagen, Michael Krystek, Jiubin Tan, and Harald Bosse. Absolute distance measurement by dual-comb interferometry with multi-channel digital lock-in phase detection. *Measurement Science and Technology*, 26:084001, 2015.
- ¹³Navid Farahi, Mehrdad Abolbashi, Jonathan Babaie, John Ziegert, Rosario Porras-Aguilar, Angela Davies, and Faramarz Farahi. Inverse projected-fringe technique for measurement of dimensions and surface profile of axisymmetric objects. *Measurement Science and Technology*, 30:015009, 2018.
- ¹⁴BP Abbott, R Abbott, R Adhikari, P Ajith, Bruce Allen, G Allen, RS Amin, SB Anderson, WG Anderson, MA Arain, et al. LIGO: the laser interferometer gravitational-wave observatory. *Reports on Progress in Physics*, 72:076901, 2009.
- ¹⁵Benjamin P Abbott, Richard Abbott, TDe Abbott, MR Abernathy, Fausto Acernese, Kendall Ackley, Carl Adams, Thomas Adams, Paolo Addesso, Rana X Adhikari, et al. Observation of gravitational waves from a binary black hole merger. *Physical Review Letters*, 116:061102, 2016.
- ¹⁶Yunxiao Zhang, Xuan Tang, Xueshi Guo, Cui Liang, Xiaoying Li, and ZY Ou. Unbalanced Interferometer beyond Coherence Length by Amplitude Measurement. In *Quantum 2.0*, pages QTu3A–48. Optica Publishing Group, 2024.
- ¹⁷X. Gu, A. F. Kockum, A. Miranowicz, Y.-X. Liu, and F. Nori. Microwave photonics with superconducting quantum circuits. *Physics Reports*, 718-719:1–102, 2017.
- ¹⁸Alexandre Blais, Arne L Grimsmo, Steven M Girvin, and Andreas Wallraff. Circuit quantum electrodynamics. *Reviews of Modern Physics*, 93:025005, 2021.
- ¹⁹P. Adhikari, M. Hafezi, and J. M. Taylor. Nonlinear Optics Quantum Computing with Circuit QED. *Physical Review Letters*, 110:060503, 2013.
- ²⁰D. Roy, C. M. Wilson, and O. Firstenberg. Colloquium: Strongly interacting photons in one-dimensional continuum. *Reviews of Modern Physics*, 89:021001, 2017.
- ²¹Alexandra S. Shemet, Mihail I. Petrov, Ivan V. Iorsh, Alexander V. Poshakinskiy, and Alexander N. Poddubny. Waveguide quantum electrodynamics: Collective radiance and photon-photon correlations. *Reviews of Modern Physics*, 95:015002, 2023.
- ²²O Astafiev, Alexandre M Zagoskin, AA Abdumalikov Jr, Yu A Pashkin, T Yamamoto, K Inomata, Y Nakamura, and Jaw Shen Tsai. Resonance fluorescence of a single artificial atom. *Science*, 327:840–843, 2010.
- ²³To-Chun Hoi, CM Wilson, Göran Johansson, Tauno Palomaki, Borja Peropadre, and Per Delsing. Demonstration of a single-photon router in the microwave regime. *Physical Review Letters*, 107:073601, 2011.
- ²⁴To-Chun Hoi, Tauno Palomaki, Joel Lindkvist, Göran Johansson, Per Delsing, and CM Wilson. Generation of nonclassical microwave states using an artificial atom in 1D open space. *Physical Review Letters*, 108:263601, 2012.
- ²⁵P. Y. Wen, O. V. Ivakhnenko, M. A. Nakonechnyi, B. Suri, J.-J. Lin, W.-J. Lin, J. C. Chen, S. N. Shevchenko, Franco Nori, and I.-C. Hoi. Landau-Zener–Stückelberg–Majorana interferometry of a superconducting qubit in front of a mirror. *Physical Review B*, 102:075448, 2020.
- ²⁶Io-Chun Hoi, Anton F Kockum, Tauno Palomaki, Thomas M Stace, Bixuan Fan, Lars Tornberg, Sankar R Sathyamoorthy, Göran Johansson, Per Delsing, and CM Wilson. Giant cross-Kerr effect for propagating microwaves induced by an artificial atom. *Physical Review Letters*, 111:053601, 2013.

- ²⁷I-C Hoi, A Frisk Kockum, L Tornberg, A Pourkabirian, G Johansson, Per Delsing, and CM Wilson. Probing the quantum vacuum with an artificial atom in front of a mirror. *Nature Physics*, 11:1045–1049, 2015.
- ²⁸Y.-T. Cheng, C.-H. Chien, K.-M. Hsieh, Y.-H. Huang, P. Y. Wen, W.-J. Lin, Y. Lu, F. Aziz, C.-P. Lee, K.-T. Lin, C.-Y. Chen, J. C. Chen, C.-S. Chuu, A. F. Kockum, G.-D. Lin, Y.-H. Lin, and I.-C. Hoi. Tuning atom-field interaction via phase shaping. *Physical Review A*, 109:023705, 2024.
- ²⁹PY Wen, AF Kockum, H Ian, JC Chen, F Nori, and I-C Hoi. Reflective amplification without population inversion from a strongly driven superconducting qubit. *Physical Review Letters*, 120:063603, 2018.
- ³⁰PY Wen, K-T Lin, AF Kockum, B Suri, H Ian, JC Chen, SY Mao, CC Chiu, P Delsing, F Nori, et al. Large collective Lamb shift of two distant superconducting artificial atoms. *Physical Review Letters*, 123:233602, 2019.
- ³¹M. P. Liul, C.-H. Chien, C.-Y. Chen, P. Y. Wen, J. C. Chen, Y.-H. Lin, S. N. Shevchenko, Franco Nori, and I.-C. Hoi. Coherent dynamics of a photon-dressed qubit. *Physical Review B*, 107:195441, 2023.
- ³²Bharath Kannan, Max J Ruckriegel, Daniel L Campbell, Anton Frisk Kockum, Jochen Braumüller, David K Kim, Morten Kjaergaard, Philip Krantz, Alexander Melville, Bethany M Niedzielski, et al. Waveguide quantum electrodynamics with superconducting artificial giant atoms. *Nature*, 583:775–779, 2020.
- ³³Arjan F Van Loo, Arkady Fedorov, Kevin Lalumiere, Barry C Sanders, Alexandre Blais, and Andreas Wallraff. Photon-mediated interactions between distant artificial atoms. *Science*, 342:1494–1496, 2013.
- ³⁴Wei-Ju Lin, Yong Lu, Ping Yi Wen, Yu-Ting Cheng, Ching-Ping Lee, Kuan Ting Lin, Kuan Hsun Chiang, Ming Che Hsieh, Ching-Yeh Chen, Chin-Hsun Chien, et al. Deterministic loading of microwaves onto an artificial atom using a time-reversed waveform. *Nano Letters*, 22:8137–8142, 2022.
- ³⁵Julien Gabelli, L-H Reydellet, Gwendal Feve, J-M Berroir, Bernard Placais, Patrice Roche, and D Christian Glattli. Hanbury brown–twiss correlations to probe the population statistics of ghz photons emitted by conductors. *Physical review letters*, 93(5):056801, 2004.
- ³⁶M. Mariani, M. J. Storcz, F. K. Wilhelm, W. D. Oliver, A. Emmert, A. Marx, R. Gross, H. Christ, and E. Solano. On-Chip Microwave Fock States and Quantum Homodyne Measurements, 2005.
- ³⁷D. M. Pozar. *Microwave Engineering*. John Wiley & Sons, Inc., 4 edition, 2011.
- ³⁸M. Mariani, E. P. Menzel, F. Deppe, M. A. Araque Caballero, A. Baust, T. Niemczyk, E. Hoffmann, E. Solano, A. Marx, and R. Gross. Planck Spectroscopy and Quantum Noise of Microwave Beam Splitters. *Physical Review Letters*, 105:133601, 2010.
- ³⁹B. Abdo, K. Sliwa, F. Schackert, N. Bergeal, M. Hatridge, L. Frunzio, A. D. Stone, and M. Devoret. Full Coherent Frequency Conversion between Two Propagating Microwave Modes. *Physical Review Letters*, 110:173902, 2013.
- ⁴⁰Jens Koch, Terri M Yu, Jay Gambetta, Andrew A Houck, David I Schuster, Johannes Majer, Alexandre Blais, Michel H Devoret, Steven M Girvin, and Robert J Schoelkopf. Charge-insensitive qubit design derived from the Cooper pair box. *Physical Review A*, 76:042319, 2007.
- ⁴¹Alexandre Roulet, Huy Nguyen Le, and Valerio Scarani. Two photons on an atomic beam splitter: Nonlinear scattering and induced correlations. *Physical Review A*, 93:033838, 2016.
- ⁴²D. Oehri, M. Pletyukhov, V. Gritsev, G. Blatter, and S. Schmidt. Tunable, nonlinear Hong-Ou-Mandel interferometer. *Physical Review A*, 91:033816, 2015.
- ⁴³Supplementary material.
- ⁴⁴Christopher C Gerry and Peter L Knight. *Introductory quantum optics*. Cambridge University Press, 2023.
- ⁴⁵Yong Lu, Andreas Bengtsson, Jonathan J Burnett, Emely Wiegand, Baladitya Suri, Philip Krantz, Anita Fadavi Roudsari, Anton Frisk Kockum, Simone Gasparinetti, Göran Johansson, et al. Characterizing decoherence rates of a superconducting qubit by direct microwave scattering. *npj Quantum Information*, 7:35, 2021.

Supplementary Material for “Tunable coherent microwave beam splitter and combiner at the single-photon level”

Y.-H. Huang,^{1, a)} K.-M. Hsieh,^{2, a)} F. Aziz,^{1, a)} Z. Q. Niu,^{3, 4, a)} P. Y. Wen,⁵
Y.-T. Cheng,² Y.-S. Tsai,¹ J. C. Chen,^{1, 6} Xin Wang,² A. F. Kockum,⁷ Z.-R. Lin,^{3, b)}
Y.-H. Lin,^{1, 6, b)} and I.-C. Hoi^{1, 2, b)}

¹⁾*Department of Physics, National Tsing Hua University, Hsinchu 30013, Taiwan*

²⁾*Department of Physics, City University of Hong Kong, Kowloon, Hong Kong SAR 999077, China*

³⁾*State Key Laboratory of Materials for Integrated Circuits, Shanghai Institute of Microsystem and Information Technology, Chinese Academy of Sciences, Shanghai 200050, China*

⁴⁾*ShanghaiTech University, Shanghai 201210, China*

⁵⁾*Department of Physics, National Chung Cheng University, Chiayi 621301, Taiwan*

⁶⁾*Center for Quantum Technology, National Tsing Hua University, Hsinchu 30013, Taiwan*

⁷⁾*Department of Microtechnology and Nanoscience, Chalmers University of Technology, 412 96 Gothenburg, Sweden*

^{a)}These authors contributed equally to this work.

^{b)}Corresponding authors: zrlin@mail.sim.ac.cn, yhlin@phys.nthu.edu.tw, iochoi@cityu.edu.hk

CONTENTS

S1. Details of the experimental setup	3
S2. Single-tone spectroscopy in the frequency domain	4
S3. Calibration measurements in the time domain	6
S4. Calculation of the scattering matrix	7
S5. Beam-splitter switching in the time domain	8
S6. Detailed data for the beam combiner around $T = 0.5$	8
References	11

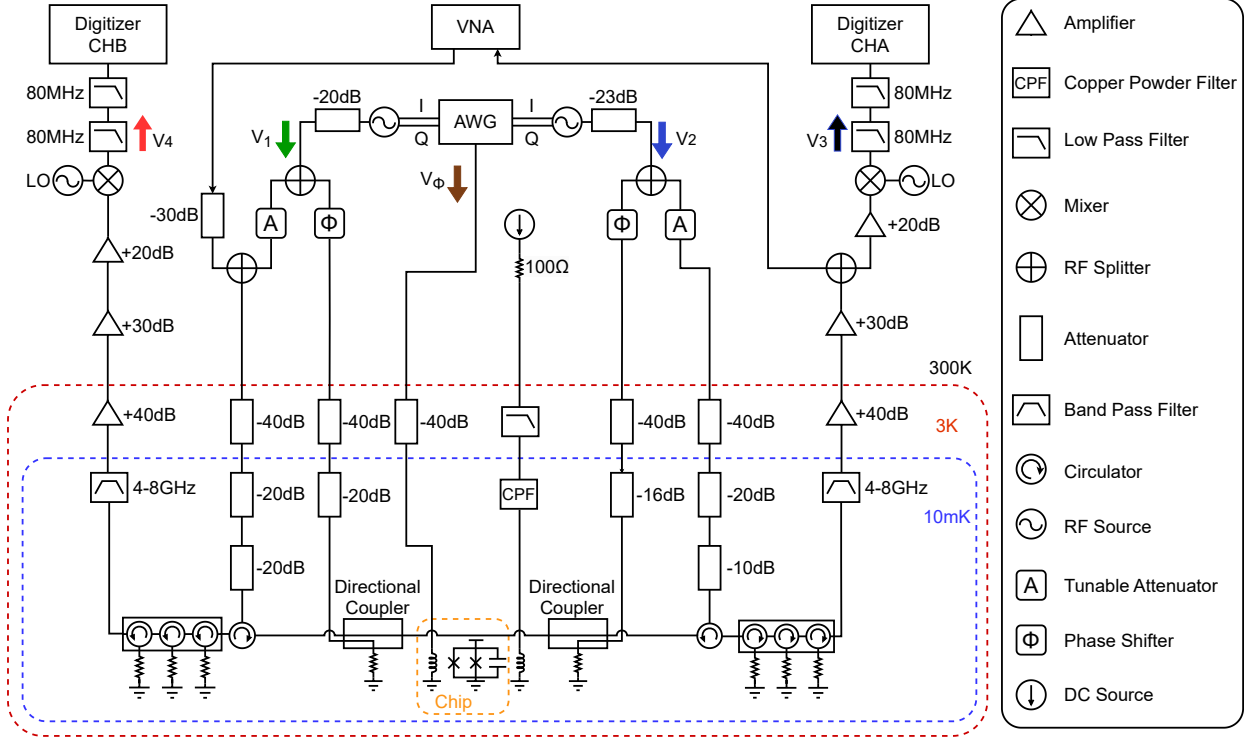


FIG. S1. Schematic of the experimental setup. The superconducting artificial atom, a transmon qubit, is in the orange dashed box. The transmon is regulated by room-temperature electronics, including a flux line, input lines, and readout lines. The blue and red dashed boxes indicate different temperature stages within the dilution refrigerator.

S1. DETAILS OF THE EXPERIMENTAL SETUP

The experimental setup, illustrated in Fig. S1, consists of a sample box containing a chip (highlighted by an orange dashed box) that features a single artificial atom capacitively coupled to an open one-dimensional transmission line. This assembly is mounted at the bottom of a dilution refrigerator operating at a base temperature of 10 mK. A superconducting magnetic coil, centrally positioned on the sample box, is used to tune the resonance frequency of the artificial atom. This coil is controlled by a DC source at room temperature, connected through a low-pass filter (LPF) and a copper powder filter (CPF) for noise filtering. The experimental setup is symmetrically arranged on both sides of the sample box to facilitate both frequency-domain and time-domain measurements, supporting our beam-splitter and beam-combiner experiments.

Single-tone spectroscopy is conducted using a vector network analyzer (VNA) to characterize the qubit, detailed further in Sec. S2. During these experiments, a weak probe field is introduced

through the VNA at a probe frequency ω_p , attenuated at several stages within the dilution refrigerator. A cryogenic circulator then directs this input field to interact with the qubit. The field transmitted from the qubit is captured by the VNA after passing through a series of cryogenic circulators, a band-pass filter (BPF), and a two-stage amplification process involving a high-electron-mobility transistor (HEMT) amplifier at 3 K and another amplifier at room temperature.

For time-domain measurements, an arbitrary waveform generator (AWG) generates IQ signals for the IQ modulator of the radio-frequency (RF) source to produce shaped modulation signals. The modulation signals are input as a pulse on the left side (V_1 , green arrow), and/or a continuous wave on the right side (V_2 , blue arrow). The output signals, V_3 (black arrow) and V_4 (red arrow), on both sides are measured at digitizer channels *A* and *B* (CHA and CHB), respectively. Additionally, an RF splitter is utilized at the input sides of the modulation signals. One of the split fields is routed to the cryogenic circulator through several attenuators and a tunable attenuator, denoted by *A*, at room temperature. The other field is connected to the directional coupler through several attenuators and a phase shifter, denoted as Φ , at room temperature. This configuration mitigates leakage from the imperfect isolation of the circulators. The detailed procedure for cancellation of leakage fields can be found in Ref.^{S1}. The near-perfect cancellation of leakage field can be seen in Fig. 3 [V_3 ($V_{2,\text{in}}$ w/o qubit) and V_4 ($V_{1,\text{in}}$ w/o qubit)] in the main text. The local flux through the chip (inside the orange-dashed box) is controlled by the AWG via the V_Φ line (brown arrow) for fast switching, with a -40 dB attenuation at 3 K.

S2. SINGLE-TONE SPECTROSCOPY IN THE FREQUENCY DOMAIN

To characterize the parameters of the qubit, we conducted single-tone spectroscopy. Fig. S2(a) illustrates the magnitude of the transmission coefficient, $|t|$, as a function of the probe frequency ω_p and the current I applied in the superconducting coil to control the global flux that sets the transition frequencies of the transmon. The spectrum reveals the cosine dependence on the flux of the qubit's $|0\rangle \leftrightarrow |1\rangle$ transition frequency. We note that a stray cavity resonance is visible at $\omega_p/2\pi = 5.425$ GHz, accompanied by additional box modes appearing as vertical lines near the stray cavity and the apex. To avoid interference from these modes, we selected a biasing point for our beam-splitter and -combiner experiments at $\omega_p/2\pi = 4.1108$ GHz, marked by a red arrow.

In Fig. S2(b), the transmission coefficient is depicted in the IQ plane for weak probe power P_p , where the Rabi frequency Ω is significantly smaller than the decoherence rate γ , resulting

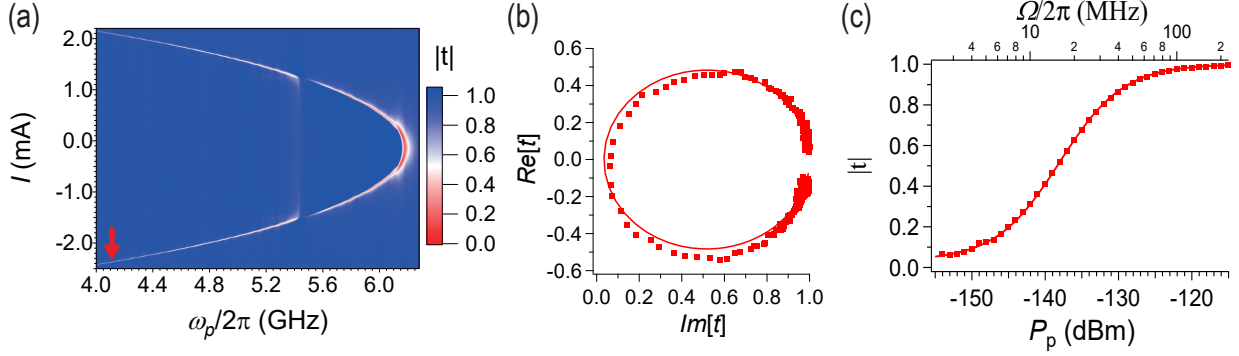


FIG. S2. Single-tone frequency-domain measurement of the transmission coefficient. (a) Transmission coefficient as a function of probe frequency ω_p and the current I controlling the flux through the SQUID of the transmon qubit. (b) Transmission coefficient plotted in the IQ plane for a weak probe (i.e., assuming $\Omega \ll \gamma$). (c) The on-resonance transmission magnitude $|t|$ as a function of probe power $P_p (\propto \Omega^2)$. The solid curves in panels (a) and (b) are theory using Eqs. (4) and (5) in the main text.

E_C/h	E_J/h	E_J/E_C	$\omega/2\pi$	$\Gamma/2\pi$	$\Gamma^n/2\pi$	$\gamma/2\pi$	ϕ
[MHz]	[GHz]	-	[GHz]	[MHz]	[MHz]	[MHz]	[rad]
199.4	25.57	128.24	4.1108	22.15	0.39	11.47	0.0526

TABLE S1. Extracted qubit parameters. We obtain the resonance frequency ω , the relaxation rate Γ , and the decoherence rate γ from Fig. S2(b) by circle fitting in the IQ plane^{S2,S3}. The non-radiative decay rate Γ^n is calculated using $\gamma = \Gamma/2 + \Gamma^n$. We extracted the anharmonicity between the $|0\rangle \leftrightarrow |1\rangle$ and $|1\rangle \leftrightarrow |2\rangle$ transitions from two-tone spectroscopy^{S4}. The anharmonicity approximately equals the charging energy E_C ^{S5}. ϕ is the mismatch angle due to the impedance mismatch from the transmission lines.

in a circular pattern. The experimental data points are indicated by red markers, while the solid curve represents the theoretical circle fit^{S2,S3}, from which we extract the parameters ω , Γ , and γ , all summarized in Table S1. Note that we have accounted for impedance mismatch ϕ in both the theoretical curve and the experimental data in Fig. S2(b)-(c).

Additionally, Fig. S2(c) displays the magnitude of the transmission coefficient, $|t|$, as a function of P_p at the resonance frequency of the qubit. For low probe power, the incident coherent field undergoes extinction by up to 94.7% in amplitude. With increasing probe power, a strong non-linearity emerges, saturating the qubit at high probe powers and leading to a unity transmission coefficient^{S6}. The experimental data points are marked with red markers, and the theoretical fit is

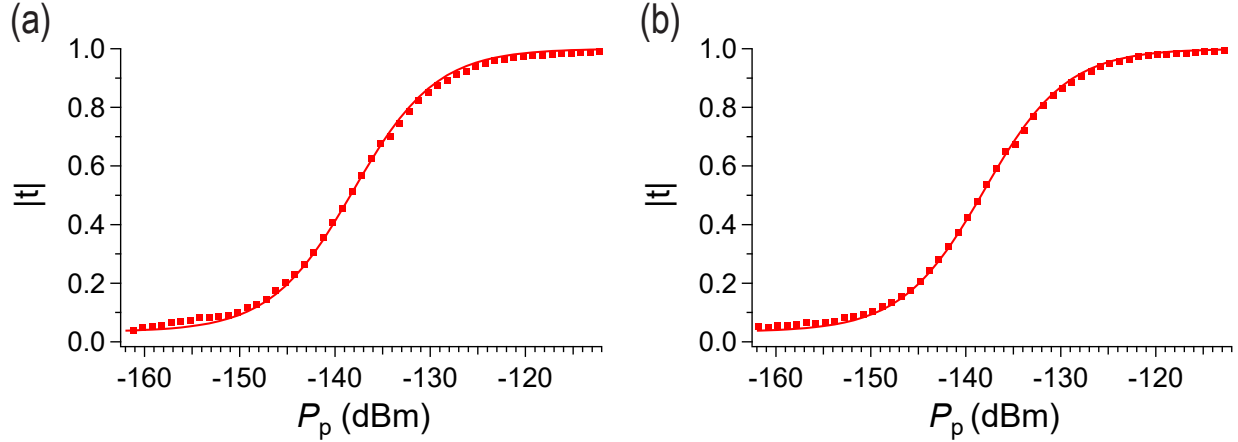


FIG. S3. The magnitude of the transmission coefficient, $|t|$, as a function of probe power P_p (converted from time domain) when the probe is resonant with the qubit. The figure displays both measured data points (markers) and theoretical fits (solid curves). (a) Measurements taken on digitizer channel A, with the input port located on the left side of the AWG, indicated by V_1 (green arrow) in Fig. S1. (b) Measurements taken on digitizer channel B, with the input port located on the right side of the AWG, indicated by V_2 (blue arrow) in Fig. S1.

shown with a solid curve. All extracted parameters are summarized in Table S1.

S3. CALIBRATION MEASUREMENTS IN THE TIME DOMAIN

To calibrate the gain and the attenuation of the input-output lines, we employ a time-domain setup as illustrated in Fig. S1 and perform single-tone calibration measurements. We bias our qubit at a resonance frequency of $\omega/2\pi = 4.1108$ GHz and apply a pulse with a duration of $2\mu\text{s}$. This duration is chosen to ensure that the qubit reaches a steady state, enabling us to obtain the average on-resonance signal in the steady state, $\langle V_{t,\text{on}} \rangle$, across various probe powers. Similarly, we conduct experiments with the qubit significantly far detuned to measure the average off-resonance signal $\langle V_{t,\text{off}} \rangle$. The magnitude of the transmission coefficient $|t|$ is calculated as

$$|t| = \left| \frac{\langle V_{t,\text{on}} \rangle}{\langle V_{t,\text{off}} \rangle} \right|. \quad (\text{S1})$$

Figure S3(a) presents measurement results across different probe powers, where the input port is connected to the left side of the AWG, as indicated by the green arrow, and the transmitted output is captured on digitizer channel A in Fig. S1. Conversely, Fig. S3(b) features the input connected

Frequency domain		Time domain			
A_{freq}	G_{freq}	A_{ChA}	G_{ChA}	A_{ChB}	G_{ChB}
-125.05 dB	69.13 dB	-132.06 dB	89.77 dB	-132.82 dB	92.22 dB

TABLE S2. Extracted gain G and attenuation A from frequency- and time-domain measurements^{S7}. In the time-domain results, subscripts with ChA refer to calibration measurements taken on digitizer channel A with the input port for V_1 , as shown in Fig. S3(a). Subscripts with ChB refer to measurements taken on digitizer channel B with the input port for V_2 , as shown in Fig. S3(b).

to the right side of the AWG, as indicated by the blue arrow in Fig. S1, with the transmitted output captured on digitizer channel B. The experimental data points are marked in red, while the solid curves represent theoretical fits using Eqs. (4) and (5) in the main text. Based on the method described in Ref.^{S7}, we can determine the gain and attenuation in time-domain measurements. For frequency-domain measurements, using the same fitting method as in Fig. S2(c), we can also determine the gain and attenuation. All extracted gain and attenuation are summarized in Table S2.

S4. CALCULATION OF THE SCATTERING MATRIX

In this section, we discuss the calculations for the elements of the scattering matrix. Initially, we detune the qubit far away, resulting in full transmission ($t = 1$) for diagonal terms and no reflection ($r = 0$) for off-diagonal terms. The scattering matrix can then be expressed as

$$\begin{pmatrix} V_3 \\ V_4 \end{pmatrix} = \begin{pmatrix} 1 & 0 \\ 0 & 1 \end{pmatrix} \begin{pmatrix} V_1 \\ 0 \end{pmatrix} \quad (\text{S2})$$

when the only input is the V_1 pulse ($V_2 = 0$). Here, $V_3 = V_1$, as depicted in Fig. 1(a) of the main text. Similarly, we obtain $V_4 = V_2$ when $V_1 = 0$:

$$\begin{pmatrix} V_3 \\ V_4 \end{pmatrix} = \begin{pmatrix} 1 & 0 \\ 0 & 1 \end{pmatrix} \begin{pmatrix} 0 \\ V_2 \end{pmatrix}. \quad (\text{S3})$$

When the qubit interacts with the field, the scattering matrix includes t_L and t_R as diagonal terms, and r_L and r_R as off-diagonal terms. The subscripts ‘‘R’’ and ‘‘L’’ denote ‘‘right’’ and ‘‘left’’, respectively, referring to the direction relative to the sample. The scattering matrix becomes

$$\begin{pmatrix} V_3 \\ V_4 \end{pmatrix} = \begin{pmatrix} t_L & r_R \\ r_L & t_R \end{pmatrix} \begin{pmatrix} V_1 \\ 0 \end{pmatrix}. \quad (\text{S4})$$

when only the V_1 pulse is used as input; we then obtain $V_3 = t_L V_1$ and $V_4 = r_L V_1$. Conversely, with $V_1 = 0$ and $V_2 = V_2$, we find $V_3 = r_R V_2$ and $V_4 = t_R V_2$:

$$\begin{pmatrix} V_3 \\ V_4 \end{pmatrix} = \begin{pmatrix} t_L & r_R \\ r_L & t_R \end{pmatrix} \begin{pmatrix} 0 \\ V_2 \end{pmatrix} \quad (\text{S5})$$

Through these calculations, we derive the coefficients r_R , t_R , r_L , and t_L , representing the right reflection, right transmission, left reflection, and left transmission coefficients, respectively, within the scattering matrix. These parameters are summarized in Table II in the main text for Fig. 3(a). These coefficients provide valuable insights for evaluating the interference effects between the input pulses. Utilizing these coefficients, we simulate the theoretical results, allowing us to compare and validate experimental observations with theoretical predictions.

S5. BEAM-SPLITTER SWITCHING IN THE TIME DOMAIN

In this section, we present the detailed results of Fig. 2(b) from the main text, shown in Fig. S4. First, we biased the qubit at $\omega/2\pi = 4.2108$ GHz (far detuned). Then, we varied the local flux by applying Gaussian pulses of varying amplitudes V_Φ , as depicted on the y axis in Fig. S4. We continuously probed the system using a continuous wave at a frequency of $\omega_p/2\pi = 4.1108$ GHz with weak probe power. The pulse length is represented on the x axis.

In Fig. S4(a)-(b), a noticeable change in the power ratio (indicated by a shift in color) occurs as we sweep the amplitude of the local flux, which adjusts the $|0\rangle \leftrightarrow |1\rangle$ transition frequency of the qubit. Near 220 mV (indicated by a dashed line), we reach a 50:50 ratio (meaning that the system acts as a 50/50 beam splitter), similar to what is observed when the qubit is biased at $\omega/2\pi = 4.12$ GHz in Fig. 2(a) of the main text (highlighted by a purple arrow). As we further increase the amplitude of the local flux, the power ratio shifts towards 0 and 1, corresponding to the qubit being on resonance at $\omega/2\pi = 4.1108$ GHz, with complementary values appearing in the lower region where the qubit is far detuned. This technique allows for switching the beam splitter in nanoseconds.

S6. DETAILED DATA FOR THE BEAM COMBINER AROUND $T = 0.5$

In this section, we present the detailed interference data of Fig. 3(a) in the main text. As mentioned, we set the qubit's resonance frequency to $\omega/2\pi = 4.12$ GHz to achieve a transmittance

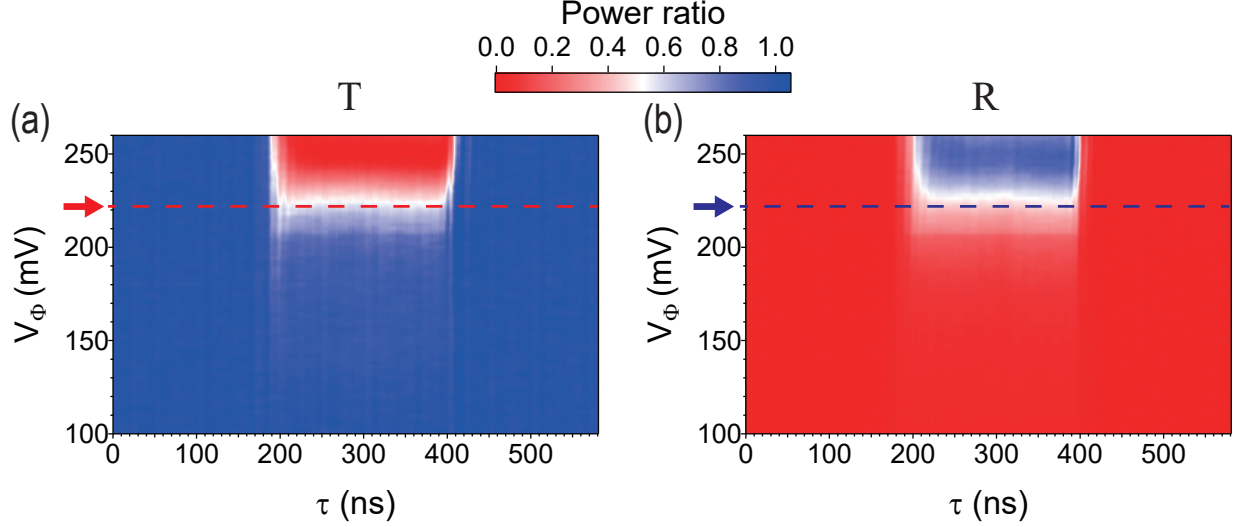


FIG. S4. Power ratio (transmittance and reflectance) for the output signals as a function of time and of the flux-biasing amplitude V_Φ at weak probe power ($\Omega \ll \gamma$). (a) Transmittance T measured using digitizer channel A. (b) Reflectance R measured using digitizer channel B. A continuous wave is directed through one port of the open transmission line (indicated by a green arrow in Fig. S1) with a probe frequency $\omega_p/2\pi = 4.1108$ GHz at a weak probe power of -158.98 dBm. Simultaneously, a Gaussian pulse is applied to the local flux of the qubit (shown by the brown arrow in Fig. S1), with its voltage amplitude varying along the y axis, to adjust the qubit's resonance frequency, changing T and R between zero and unity (top color bar). The dashed line marks the line cut used in the main text as Fig. 2(b).

and reflectance ratio of approximately 50:50. Two weak probes (labeled V_1 and V_2) at $\omega_p/2\pi = 4.1108$ GHz are simultaneously applied to the atom with phase θ for V_1 . The output signals V_3 (V_4) are then measured using digitizer channel A (B), as shown in Fig. S5(a)-(b).

We extract and average the steady-state signal from the data corresponding to τ from 50 to 150 ns for each θ case. This yields the blue (red) data points in Fig. 3(a) in the main text. The experimental data matches well with the simulation results in Fig. S5(c)-(d).

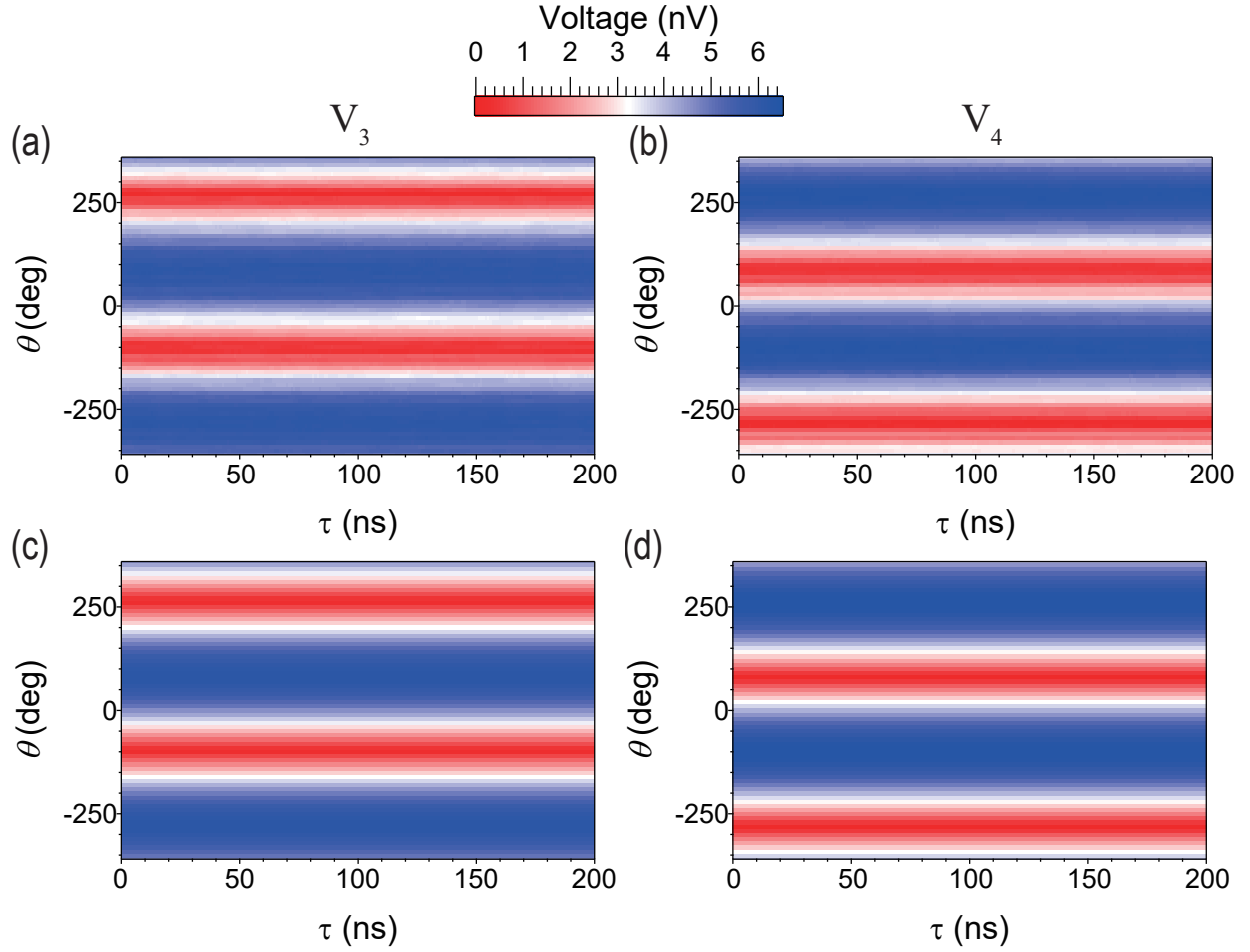


FIG. S5. Beam-combiner results around $T = 0.5$, as a function of time τ and the phase θ of the input V_1 . (a) V_3 output signal measured using digitizer channel A. (b) V_4 output signal measured using digitizer channel B. (c, d) Theoretical simulations corresponding to panels (a) and (b), respectively, based on Eqs. (1)–(5) from the main text, using the parameters listed in Table II of the main text.

REFERENCES

- [S1] I.-C. Hoi, C. M. Wilson, G. Johansson, J. Lindkvist, B. Peropadre, T. Palomaki, and P. Delsing, “Microwave quantum optics with an artificial atom in one-dimensional open space,” [New Journal of Physics](#) **15**, 025011 (2013).
- [S2] S. Probst, F. B. Song, P. A. Bushev, A. V. Ustinov, and M. Weides, “Efficient and robust analysis of complex scattering data under noise in microwave resonators,” [Review of Scientific Instruments](#) **86**, 024706 (2015).
- [S3] Y. Lu, A. Bengtsson, J. J. Burnett, E. Wiegand, B. Suri, P. Krantz, A. F. Roudsari, A. F. Kockum, S. Gasparinetti, G. Johansson, *et al.*, “Characterizing decoherence rates of a superconducting qubit by direct microwave scattering,” [npj Quantum Information](#) **7**, 35 (2021).
- [S4] I.-C. Hoi, C. Wilson, G. Johansson, J. Lindkvist, B. Peropadre, T. Palomaki, and P. Delsing, “Microwave quantum optics with an artificial atom in one-dimensional open space,” [New Journal of Physics](#) **15**, 025011 (2013).
- [S5] J. Koch, T. M. Yu, J. Gambetta, A. A. Houck, D. I. Schuster, J. Majer, A. Blais, M. H. Devoret, S. M. Girvin, and R. J. Schoelkopf, “Charge-insensitive qubit design derived from the Cooper pair box,” [Physical Review A](#) **76**, 042319 (2007).
- [S6] I.-C. Hoi, C. M. Wilson, G. Johansson, T. Palomaki, B. Peropadre, and P. Delsing, “Demonstration of a Single-Photon Router in the Microwave Regime,” [Physical Review Letters](#) **107**, 073601 (2011).
- [S7] Y.-T. Cheng, C.-H. Chien, K.-M. Hsieh, Y.-H. Huang, P. Y. Wen, W.-J. Lin, Y. Lu, F. Aziz, C.-P. Lee, K.-T. Lin, C.-Y. Chen, J. C. Chen, C.-S. Chuu, A. F. Kockum, G.-D. Lin, Y.-H. Lin, and I.-C. Hoi, “Tuning atom-field interaction via phase shaping,” [Physical Review A](#) **109**, 023705 (2024).